Triiodide Anion as a Magnesium-ion Transporter for Low Overpotential Battery Cycling in Iodine-Containing $Mg(TFSI)_2$ Electrolyte

Nathaniel Z. Hardin,† Christopher P. Woodley,† Kori D. McDonald, and Bart M. Bartlett*

Department of Chemistry, University of Michigan, Ann Arbor, MI 48109-1055 USA

Keywords: magnesium, batteries, iodine, polyiodide, overpotential

ABSTRACT: Magnesium iodide (MgI_2) solid-electrolyte interphase (SEI) layers have previously been shown to protect Mg metal anodes from passivation through products formed during $Mg(TFSI)_2$ electrolyte decomposition (TSFI = trifluorosulfonimide). MgI_2 formed *in situ* from small quantities of I_2 added to the electrolyte shows a drastic decrease in the overpotential for magnesium deposition and stripping. In this work, a MgI_2 SEI layer was created in an *ex-situ* fashion and then the electrochemical characteristics of this MgI_2 SEI layer were probed both alone, and with small quantities of I_2 or Bu_4NI_3 additives to identify the electroactive species. Chronopotentiometry (CP) and cyclic voltammetry (CV) show that the MgI_2 SEI alone is insufficient for low overpotential magnesium cycling. I(3d) XPS data show that I_3^- is formed within the SEI layer, which can serve as the electroactive species when ligated with Mg^{2+} for low overpotential (<50 mV at 0.1 mA cm^{-2} current density) cycling. Moreover, Raman shifts at 110 and 140 cm^{-1} are consistent with I_3^- formation, and these signatures are observed before and after CP experiments. The Mg^0 deposition curves in the CV with additives are consistent with a diffusive species. Finally, electrochemical impedance spectroscopy (EIS) shows that there is a large decrease in the charge-transfer resistance within the SEI when either I_2 or Bu_4NI_3 additives are used, which supports a solvating effect that facilitates magnesium deposition and stripping.

Introduction

As the world moves from fossil fuels to renewable energy, there is a rising demand for new energy storage technologies. [1] One promising strategy is the rechargeable magnesium battery which incorporates magnesium metal anodes, possessing higher volumetric capacity (3833 mAh mL^{-1} vs. 2062 mAh mL^{-1}), greater abundance, and improved safety due to less reactivity towards moisture when compared to current lithium technology.[2-5] However, magnesium batteries have two main scientific limitations that have impeded their widespread use and development: (1). the lack of high energy density cathode materials with suitable intercalation kinetics to pair with magnesium metal anodes,[6,7] and (2). developing magnesium-containing electrolytes that are compatible with magnesium metal anodes.[8-10] Currently, magnesium battery electrolytes are targeted for reversible magnesium stripping/deposition with the development of complex Grignard-based electrolytes first proposed in 2000 by the Aurbach group.[11] Since then, electrolytes based on phenyls , alkoxides, boron, fluorinated alkoxide, and Mg salt electrolytes have been discovered, along with polymer electrolytes.[8,12-15] Although Grignard based electrolytes are reductively stable and have achieved high coulombic efficiencies, they incorporate strong Lewis acids such as aluminum chloride, providing a corrosive chloride source that damages metal current collectors.[16,17] Grignard-free electrolytes have been developed, yet many still rely on a strong Lewis acids and still frequently include chloride ions.[18,19] These electrolytes are effective in cycling magnesium with low overpotentials and afford long term stability, but their complicated syntheses, extreme sensitivity to air and moisture, high corrosiveness, and incompatibility with oxide based cathodes outlined the need to develop magnesium simple salt electrolytes incorporating anions such as $TFSI^-$, ClO_4^-, and PF_6^-.[7]

Simple salt electrolytes are incredibly attractive for magnesium batteries, but they typically display reductive incompatibility with magnesium metal anodes, leading to electrolyte decomposition that gives rise to forming a passivating layer, which then results in high overpotentials for cycling.[20,21] Furthermore, many aprotic solvents used in lithium batteries that allow for high conductivity, such as alkyl carbonates, also decompose on the magnesium metal anode and form a passivation layer.[22] This reductive electrolyte/solvent decomposition on magnesium metal anodes have called for extensive investigation into solid-electrolyte interfaces (SEIs). In lithium ion batteries, the SEI is formed from the electrolyte decomposition onto the lithium or graphite anode, however unlike magnesium, lithium electrolyte decomposition forms SEIs that are Li^+ conducting, while magnesium salts typically form ion-impermeable layers.[6,23] Introducing ion- and electron-conducting artificial SEIs, formed both *ex situ* or *in situ*, has been attempted, and these SEI layers inhibit electrolyte decomposition on magnesium metal anodes, with examples including Li-derived SEIs, polymer SEIs and Mg-halide SEIs.[24-26]

Mg-halide SEIs have received attention due to their ease of preparation and reductive stability. A promising 2017 report describes *in situ* MgI_2 SEI formation upon cycling in I_2-containing electrolytes; magnesium deposition and stripping overpotentials were vastly reduced, and long-term cycling stability was observed.[27,28] Wang and co-workers reported that upon adding I_2 to a 0.5 M $Mg(TFSI)_2$ electrolyte in dimethoxyethane (DME) solvent, a MgI_2 layer formed, characterized by X-ray photoelectron spectroscopy (XPS); the I^- (3d) signal increased as higher concentrations of I_2 were added to the electrolyte.[28] Furthermore, an increase in I_2 concentration from 1 mM to 50 mM greatly decreased the magnesium stripping overpotential from 1.87 V to 0.05 V vs Mg/Mg^{2+}. Comparing this work with other research in rechargeable magnesium batteries revealed a key

discrepancy. Fichtner and co-workers used density functional theory (DFT) to calculate formation energies of MgI_2, which were found to be larger than expected, and make the explanation for low overpotentials reported by Wang *et al.* unsatisfactory.[29] In this work, we aim to resolve the outstanding discrepancy and to identify the underlying mechanism resulting in low overpotential cycling with MgI_2 SEIs.

Results and Discussion

Characterizing the MgI_2 SEI

An MgI_2 SEI layer was deposited by the spontaneous chemical reduction of iodine onto magnesium foil in hexanes (see experimental section) to assess the electrochemistry of the MgI_2-coated electrode. The reaction is:

$$\text{Mg (excess)} + I_2 \rightarrow \text{Mg|MgI}_2 \quad (1)$$

where the notation for the product emphasizes that MgI_2 coats the Mg metal to form an interface. The X-ray diffraction (XRD) pattern of the resulting electrode shows only the underlying magnesium metal, indicating that the MgI_2 is amorphous (Figure S1). Therefore, scanning electron microscopy (SEM) and energy-dispersive X-ray (EDX) analysis were used to characterize the Mg|MgI_2 interface, illustrated in **Figure 1 (**with the EDX spectrum provided as Figure S2). Notable is that the MgI_2 layer is 6 – 10 µm thick, and iodine is present only in this layer.

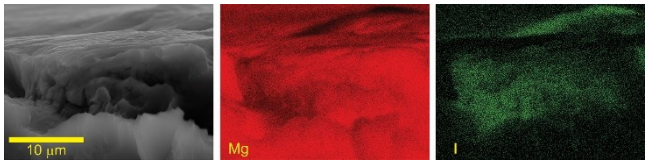

Figure 1. Cross-sectional SEM image of the MgI_2 layer deposited onto Mg metal with EDX maps of magnesium and iodine, respectively.

Figure 2 shows two distinct ^2D lines in the I(3d) XPS, corresponding to I^- and to I_3^-, as described next. In control experiments, MgI_2 powder shows $^2D_{3/2}$ and $^2D_{5/2}$ lines at 631 and 619 eV respectively, whereas Bu_4NI_3 powder shows three distinct ^2D lines representing the multiple chemical environments for iodine in the I_3^- anion (Figure S3). I_3^- is known to have complex XP spectra due to shake-up profiles and solvent-dependent molecular geometry.[29] In the Mg|MgI_2 film, the $^2D_{3/2}$ lines at 632.3 and 630.8 eV respectively are in excellent agreement with those observed for I_3^- and I^-, respectively. Moreover, the ^2P lines in the Mg(2p) XPS shows multiple chemical environments, suggestive of MgI_2, $Mg(I_3)_2$ and MgO; the oxide forms during the transfer to the spectrometer (Figure S4). The remaining spectra in Figure 2 show that the SEI surface layer is dynamic, but that signatures for I_3^- remain regardless of what other species are included in the electrolyte mixture.

The XPS results suggest that I_2 reacts with I^- within the MgI_2 SEI to form I_3^-, described by the balanced equation:

$$I_2 + I_I^{\times} \rightleftharpoons I_{3i}' + V_I^{\bullet} \quad (2)$$

in Kroger-Vink notation, where $I_I^{\times}$ is iodide present in the MgI_2 SEI, I_{3i}' is interstitial (or adsorbed) I_3^-, and $V_I^{\bullet}$ is an iodide vacancy left behind for charge balance. In **Scheme 1**, we propose a mechanism by which a neutral MgI_2 SEI is permeable to both Mg^{2+} and I_3^- ions. These ions form a transient complex facilitating lower overpotential deposition and stripping. The low

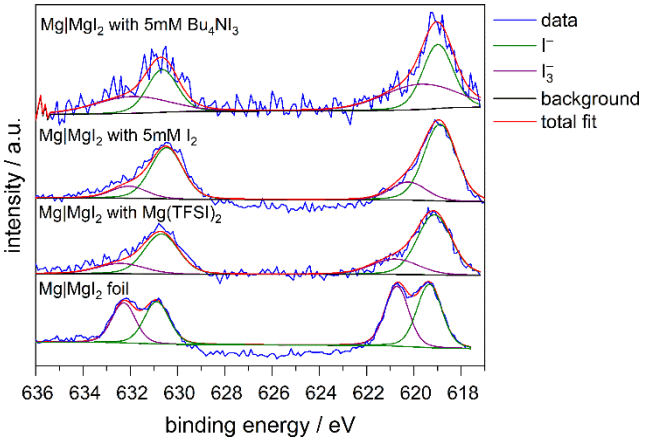

Figure 2. I(3d) XPS of Mg|MgI_2 Mg foil electrodes used in this study.

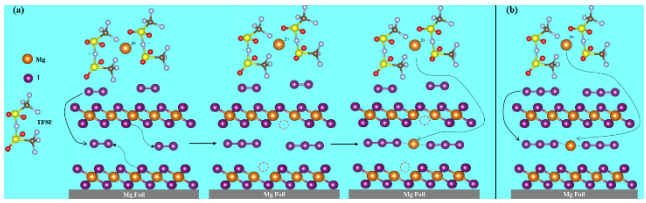

Scheme 1. a) Proposed mechanism of I_2 absorption and subsequent reaction with the MgI_2 SEI to form I_3^- and subsequent role I_3^- plays in Mg^{2+} complexation in the SEI layer. b) Proposed mechanism of I_3^- absorption and subsequent role I_3^- plays in Mg^{2+} complexation in the SEI layer. This Scheme was created using VESTA and Avogadro. [30,31]

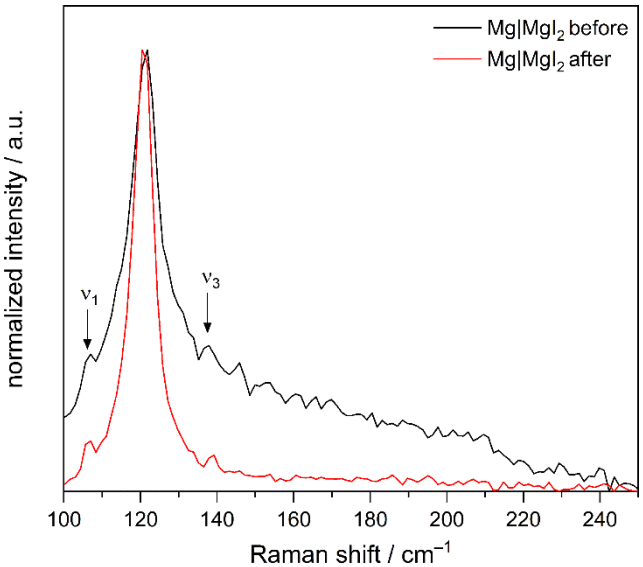

Figure 3. Raman spectra of MgI_2 SEI surfaces wet with electrolyte before and after galvanostatic cycling.

concentration of iodine additives and the equilibrium reaction in equation 2 results in minimal local changes to the MgI_2 SEI as ions are intercalated and deintercalated. We note that although $Mg(I_3)_2$ is unstable with respect to disproportionation, I_3^- has been observed to form at the cathode of Mg-I_2 batteries and alters the solubility of MgI_2.[32]

Raman spectroscopy provides further evidence for forming I_3^- on the Mg|MgI_2 electrodes. **Figure 3** shows the characteristic

Raman shifts for I_3^- (ν_1 at 110 cm^{-1}, and ν_3 at 140 cm^{-1}). In these spectra a large MgO mode at 120 cm^{-1} results from exposing the film to air. Important is that these I_3^- Raman signatures remain *after* the galvanostatic cycling experiments detailed in the next section.

Galvanostatic Cycling of Symmetric Cells.

To understand the influence of the a MgI_2 SEI on the overpotential for magnesium deposition/stripping in $Mg(TFSI)_2$ electrolyte, we carried out four chronopotentiometry (CP) (i.e. – galvanostatic cycling) experiments—all using symmetric Swagelok™ cells in bis(2-methoxyethyl) ether (diglyme) solvent containing 0.5 M $Mg(TFSI)_2$ at a current density of 0.1 mA cm^{-2}: 1) using pristine magnesium metal as the working electrode (Mg in $Mg(TFSI)_2$ electrolyte solution); 2) using the $Mg|MgI_2$ electrode described in the previous section in electrolyte solution; 3) using the $Mg|MgI_2$ electrode with 5 mM I_2 added to the electrolyte solution; 4) using the $Mg|MgI_2$ electrode with 5 mM Bu_4NI_3 added to the electrolyte solution. The low 5 mM additive concentration matches that in the previous report,[27] and is sufficient to allow for further equilibria between the SEI and diffusive species from solution to be observed without interfering significantly with the ionic strength of the $Mg(TFSI)_2$ electrolyte in diglyme solution. We should also note that pristine Mg metal foil was not cycled galvanostatically with either I_2 or Bu_4NI_3 additives since these additives would spontaneously react with Mg to form MgI_2.

CP data for magnesium stripping/deposition is shown in **Figure 4**, with a summary of several trials presented as Table S1. Electrode potentials are recorded (and reported throughout) relative to the $Mg^{2+/0}$ couple. The potential at which deposition and stripping occurs on pristine Mg metal is consistent with the previous literature of $Mg(TFSI)_2$ electrolyte; a large overpotential of ~ 1.89 V is observed at hour 5.[28] The $Mg|MgI_2$ electrode (i.e. – with the SEI formed first in *ex situ* fashion, followed by isolating the electrode and new preparing new cells with no additional iodine-containing species in solution during cycling) shows a small decrease in the overpotential (~1.65 V to ~1.62 V). This result conflicts with the drastically reduced overpotentials observed on electrodes with MgI_2 formed *in situ* from added I_2, suggesting that the MgI_2 SEI alone is not responsible for accelerating the rate of Mg stripping/deposition.[28] For *in situ*-generated MgI_2, higher concentrations of I_2 lead to thicker layers, and the deposition/stripping rates increase as thickness increases.[27] Either the 6 – 10 µm thick MgI_2 formed in our *ex situ* reaction limits Mg^{2+} diffusion or the authors' original assessment that MgI_2 is the responsible species is incomplete. To resolve the role of added I_2, 5 mM I_2 was added to the electrolyte. After a short conditioning period (~1 h), we observe a dramatic decrease in overpotential to ~33 mV. Adding 5 mM Bu_4NI_3 also decreases the overpotential to ~42 mV after 5 hours. These data show that merely having the MgI_2 is not the primary reason for the observed overpotential decrease, but that it results from I_3^- – *either* added directly as Bu_4NI_3 *or* from I^- (in MgI_2) reacting with I_2 in solution.

To test whether I_3^- alone will support magnesium deposition and stripping, a 274 mM $Mg(I_3)_2$ electrolyte (formed *in situ* from reacting MgI_2 and I_2 with no $Mg(TFSI)_2$) was tested with the $Mg|MgI_2$ electrodes (Figure S5). This concentration is the maximum concentration of $Mg(I_3)_2$ that is soluble in diglyme solvent. We observe no conditioning period and an a relatively low initial overpotential (~0.34 V). However, upon cycling, the overpotential increases and reaches the 5 V instrument limit

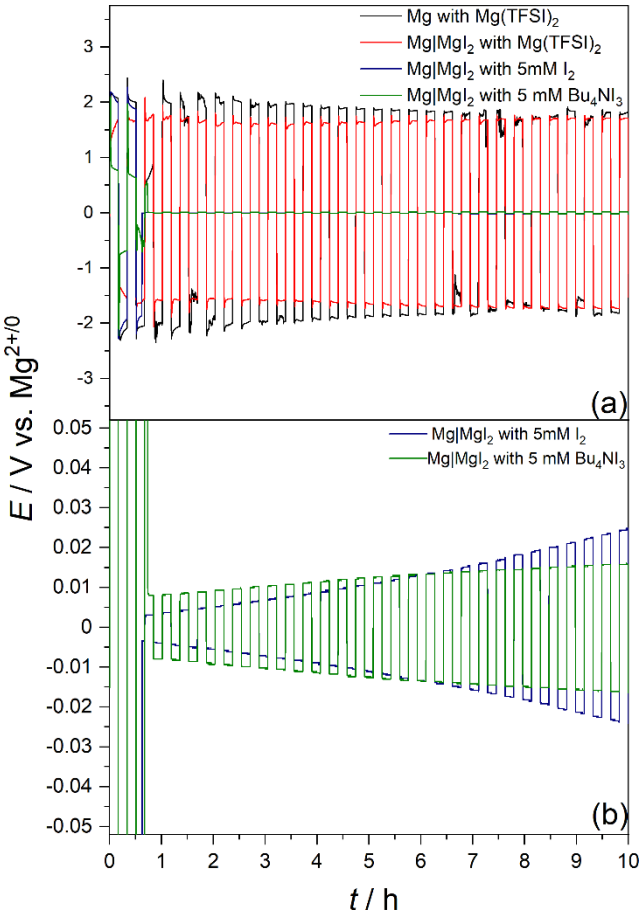

Figure 4. a) CP of symmetric Swagelok™ cells at a current density of 0.1 mA • cm^{-2} and b) magnification of the y-axis showing the low overpotential for cells with added I_2 and Bu_4NI_3.

after 8 hours. While 274 mM $Mg(I_3)_2$ electrolyte does not support long-term cycling alone, the initial low overpotential cycling indicates that $Mg(I_3)_2$ is a plausible magnesium electroactive species. Therefore, with the XPS data showing formed I_3^- within the SEI, we propose that Mg^{2+} ligated with I_3^- ion is responsible for the vastly improved Mg deposition and stripping kinetics—not Mg^{2+} diffusion through the MgI_2 layer alone. It should be noted that adding I^- directly as Bu_4NI results in salt metathesis with $Mg(TFSI)_2$ to yield insoluble MgI_2 in solution, which precipitates and therefore was not used further.

Electrochemical Characterization of Symmetric Cells.

The CP data in Figure 4 show that the overpotential for magnesium deposition and stripping decreases after the first five CP cycles when either I_2 or I_3^- is added to the $Mg(TFSI)_2$ electrolyte. However, the first few cycles show similar behavior to that observed with only MgI_2. This electrode conditioning over the first few cycles was not previously observed,[28] and cyclic voltammetry (CV) in **Figure 5** allows us to probe changes during these early conditioning cycles. Figure 5a shows that on a Mg metal electrode in $Mg(TFSI)_2$ electrolyte in diglyme solvent, the onset potential for Mg deposition increases from ~ –0.3 to ~ –1.2 V from scan 1 to scan 10, and the onset potential for Mg stripping increases from ~ 0.6 V to ~ 0.9 V, showing that as the electrodes are cycled, a passivating layer is formed, rendering the deposition and stripping of Mg more difficult.

After 10 scans, we observe a significant loss in current density, as expected with the growth of a passivating layer resulting

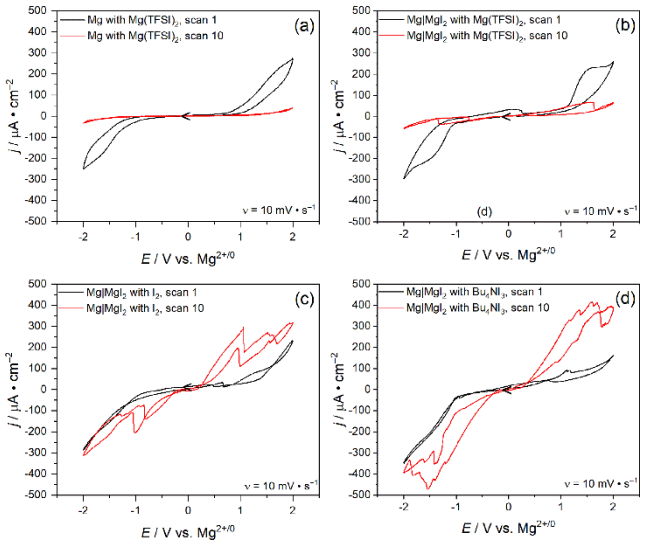

Figure 5. Cyclic voltammograms in IUPAC notation of symmetric cells at a scan rate of 10 mV/s showing scans 1 and 10 of cells containing a) Mg electrodes with $Mg(TFSI)_2$, b) $Mg|MgI_2$ electrodes with $Mg(TFSI)_2$, c) $Mg|MgI_2$ electrodes with $Mg(TFSI)_2$ and 5 mM I_2, and d) $Mg|MgI_2$ electrodes with $Mg(TFSI)_2$ and 5 mM Bu_4NI_3.

from known electrolyte $TFSI^-$ decomposition.[24,28,29,33,34] Figure 5b shows that by adding the MgI_2 SEI *ex situ,* that the onset potential for Mg stripping does not increase, while the onset potential for deposition *does* decrease over 10 scans, and there remains a decrease in current density after 10 scans. Figure 5c shows that after adding 5 mM I_2 to the $Mg(TFSI)_2$ electrolyte, a decrease in the onset potential for Mg deposition (from ~-0.3 V to ~-0.2 V for the first scan, from ~-1.2 V to -0.1 V for the 10th scan) and stripping (from ~0.6 V to ~0.4 V for the first scan, from ~0.9 V to ~ 0.1 V for the 10th scan) is observed when compared to cells with no additive. Figure 5d shows that when we add 5 mM Bu_4NI_3 to the electrolyte, the onset potentials for Mg deposition and stripping from ~–0.7 to ~ –0.2 V and from ~0.7 to ~ 0.2 V for the 1st to the 10th scan, respectively. In Figure 5c, the surface reaction between I_2 and I^- from equation 2 results in the sharp peak drop offs at approximately ± 1 V and the crossover in current at ~1.5 V. [35] After surface adsorption, the rough features can be attributed to the continued diffusion of additives to the surface. Then, in Figure 5d, we observe similar adsorption features when I_3^- is pre-formed. We note that increasing the CV scan rate from 10 mV/s to 25 mV/s (Figure S6) removes the choppiness (i.e. – diffusion limitations) but that the adsorption peaks are retained, particularly so with I_3^- in solution. We interpret the secondary peaks at lower potentials (as compared to simple $Mg(TFSI)_2$ deposition and stripping) to indicate the formation and conditioning of the $Mg|MgI_2$ SEI layer as Mg^{2+} complexes with I_3^- (Scheme 1), which allows for lower overpotential stripping/deposition in the CP experiments.

Before and after CV scanning, we conducted electrochemical impedance spectroscopy (EIS) on symmetric cells to probe the effects linked to each additive and to identify the influence that conditioning has on pristine Mg and $Mg|MgI_2$ electrodes; these data are presented in main text as **Figure 6** and in the SI as Table S2. The data are modeled using Z-view software[36] to the equivalent circuit illustrated in the figure. Of note, the Warburg (diffusion-limited) feature is included in the middle MgI_2 SEI layer, further supporting the diffusion limitations in the CV

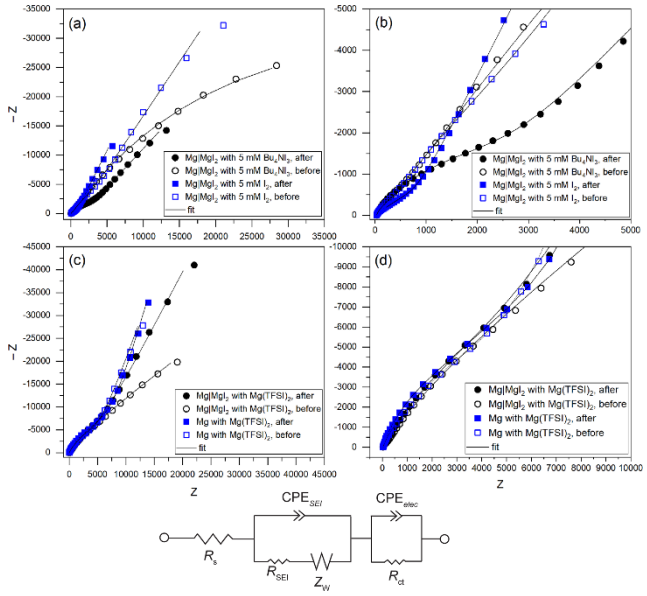

Figure 6. Nyquist plot of symmetric Swagelok™ cells with a) $Mg|MgI_2$ foil containing electrodes with I_2 and Bu_4NI_3 additives, b) zoomed in view of $Mg|MgI_2$ foil containing electrodes with I_2 and Bu_4NI_3 additives, c) Mg foil and $Mg|MgI_2$ foil containing electrodes with $Mg(TFSI)_2$, and d) zoomed in view of electrodes with no additives before and after 10 CV scans with fit and equivalent circuit used for fitting. R_s, bulk resistance of the cell (electrolyte solution, separator, and electrodes); R_{SEI}, CPE_{SEI}: resistance and capacitance of the interfacial MgI_2 layer; Z_W, Warburg diffusional effects of Mg^{2+}; R_{ct}, and CPE_{elec}: charge-transfer resistance and double-layer capacitance for Mg.

data. The modeling results show that the largest kinetic barrier is the charge-transfer resistance between the $Mg(TFSI)_2$ electrolyte and the metal electrode during the deposition and stripping reactions. For conditioning in all systems, the interfacial resistance of the SEI (R_{SEI}) increases, which is consistent with forming a new interface. Both samples containing I_2 and Bu_4NI_3 additives show a decrease in the charge-transfer resistance (R_{ct}): from 1082 Ω to 315 Ω for I_2 and 81.5 kΩ to 1.6 kΩ for Bu_4NI_3. The large decrease in R_{ct} that is seen with electrolyte containing I_2) and Bu_4NI_3 suggests that I_3^- forms a complex intermediate with Mg^{2+} that has much lower overpotential for deposition than solvated Mg^{2+} in diglyme alone. This result is shown to align with the CV data where the distinct reduction/oxidation peaks at potentials closer to the redox potential of Mg/Mg^{2+} grow in after the buildup of triiodide-ligated Mg^{2+} species with lower CT resistance.

Finally, to show that the large potential drop observed in the CP data is not due to short circuiting the electrochemical cells, we performed an experiment in which 50 CP cycles are done (Figure S7) followed by recording the post-cycling CV traces (Figure S8). From these data, we see that after SEI formation, the overpotential for Mg deposition and stripping has a range from ~2 – 30 mV for the 5 mM I_2 additive and ~40 – 200 mV for the Bu_4NI_3 additive. This range is most likely due to differences in $Mg|MgI_2$ SEI thickness from batch-to-batch preparation. Most important is that the post cycling CV traces are like those observed in Figure 5, hinting that the same electrochemical reactions are still taking place. The difference in current likely arises from the SEI dynamics with the electrochemical techniques applied.

SEM Characterization of Cycled Symmetric Cells.

In addition to the spectroscopic evidence for I_3^- formation, the influence of I_3^- complexing with Mg^{2+} to form a new electroactive species is clear from SEM analysis of the magnesium electrodes after cycling. Previous studies from our lab have shown that changing the electroactive magnesium species causes a change in magnesium deposition morphology.[37] **Figure 7** shows a stark difference in the morphology of the magnesium electrodes after cycling with and without the presence of the MgI_2 SEI and with the iodine-containing additives. Pristine magnesium metal electrodes (Figure 7a) alone show large ~20 µm size deposits, along with large pores in the electrode surface demonstrating a very uneven stripping/deposition process due to the break-up of the insulating SEI layer formed from decomposition of $TFSI^-$ and deposition of Mg into those preferential sites. When the Mg|MgI_2 surface is cycled in iodine-free solution (Figure 7b), we see ~ 10 µm size deposits with fewer large pores on the electrode surface. In stark contrast, Mg|MgI_2 electrodes cycled with I_2 or Bu_4NI_3 additive (Figures 7c and d, respectively) show a smooth, uniform surface morphology. This change in surface morphology after cycling further supports our proposed mechanism that Mg^{2+} ions interact with the SEI as triiodide-solvated species; this solvation, rather than the presence of the MgI_2 SEI, leads to more even coverage of Mg deposits as well as the enhanced deposition/stripping kinetics.

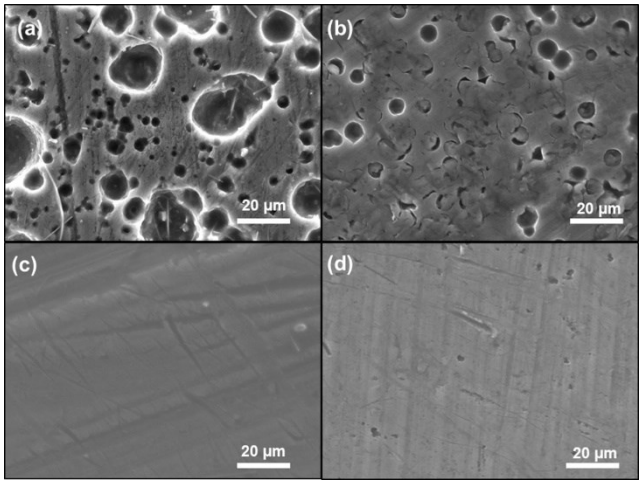

Figure 7. Top-down SEM images of Mg electrodes after galvanostatic cycling with $Mg(TFSI)_2$. a) Pristine Mg; b) Mg|MgI_2 electrode; c) Mg|MgI_2 with 5 mM I_2; and d) Mg|MgI_2 with 5 mM Bu_4NI_3.

To further probe the electrochemical characteristics of the Mg|MgI_2 layer, galvanostatic intermittent titration technique (GITT) experiments were performed (Figure S9). A 15 cycle galvanostatic conditioning period was first performed followed by a 1 minute, 0.1 mA/cm^2 charge pulse with a 3-minute rest period for 50 cycles followed by 50 cycles of a -0.1 mA/cm^2 discharge pulse with 3-minute rest period. Both the Bu_4I_3 and I_2 containing systems are shown to have an immediate relaxation after each pulse which is due to such high resistances as seen in the EIS. This result indicates that polarization is needed to drive Mg^{2+} ions, and significant equilibrium solid- state diffusion does not occur in the SEI, which is further supported by the Warburg element in the EIS data (Table S2) as the resistance portion decreases after 10 CV scans with all cells containing the SEI and increases for the Mg foil.

Conclusion

Cyclic voltammetry, galvanostatic cycling, and SEM imaging show that adding an *ex-situ* prepared MgI_2 SEI surface layer is not responsible for facilitated magnesium deposition and stripping in iodine-containing electrolytes. Through various spectroscopic and electrochemical methods, we were able to propose and support a novel mechanism for the known superior performance of Mg|MgI_2 electrodes. Triiodide was observed in all systems housing I_2 and I^-, and was discovered to have a latent, but profound role in the facilitation of electrochemical kinetics. The solvation effect of triiodide toward magnesium drastically reduced overpotentials for deposition and stripping, resulting in even Mg deposition on the surface of the SEI. These results show MgI_2 SEI layers protect the Mg surface from electrolyte decomposition but are not responsible for improved kinetics. Our work introduces a conceptual avenue for using triiodide in reversible magnesium battery technology and highlights the importance of tracking electroactive species in batteries.

Experimental Section

MgI_2 SEI electrode preparation: Magnesium foil was first scraped with a glass slide to remove any magnesium oxide surface layer in an Argon glovebox box (VacuumAtmosphere). The pristine magnesium foil was then transferred to a N_2 glove box (VacuumAtmosphere) and submerged in a solution of dry hexanes saturated with I_2 (600 mg I_2 stirred for 2 hours in 40 mL of hexanes and then decanted) for 12 hours. After the reaction, the I_2 saturated hexanes were removed, and the foil was washed 3x with 40 mL dry hexanes and then dried 12 hours under vacuum. The sample was then transferred to the argon box for storage. Electrodes of pristine magnesium metal and iodine treated magnesium metal were punched in discs with an area of .31 cm^2 using a hole punch.

Electrolyte preparation: $Mg(TFSI)_2$ was purchased from Strem Chemicals, Anhydrous diglyme, Bu_4NI_3, and Iodine where all purchased from Sigma Aldrich, $Mg(TFSI)_2$, was dissolved in the dry diglyme in a nitrogen box to make a 0.5 M solution. Iodine and Bu_4NI_3 additive containing electrolyte were first made by dissolving the Iodine or Bu_4NI_3 into the 0.5 M $Mg(TFSI)_2$ electrolyte to make a stock solution of 50 mM additive and 0.5 M $Mg(TFSI)_2$. The solutions were then transferred to an argon box. The working electrolyte was made by diluting the stock additive solutions with 0.5 M $Mg(TFSI)_2$ to 5 mM. 274 mM $Mg(I_3)_2$ electrolyte was formed by adding 274 mM MgI_2 and 584 mM I_2 to 1 ml diglyme and stirring overnight until complete dissolution.

Electrochemical Characterization Details: all electrochemical tests were done by using symmetric Swagelok™ cells (Figure S10) using Mg/Mg or Mg|MgI_2/Mg|MgI_2 electrodes, stainless steel current collectors and a glass fiber separator (Whatman® glass microfiber filters, Grade GF/D) which were soaked with 50 µL of electrolyte and were assembled in an argon glovebox. CVs were performed using a CH Instrument 1000A potentiostat except for the post galvanostatic cycling CVs, which used a Solartron Analytical / AMETEK SI-6200. EIS measurements were performed using an Eco Chemie Autolab PGSTAT128N potentiostat, and CP was performed using a

MTI-Neware battery analyzer. CV traces were performed for 10 forward and reverse scans in the potential range –2 V to 2 V vs $Mg^{2+/0}$ at 10 mV/s scan rate starting at 0 V vs $Mg^{2+/0}$ in the negative direction. EIS measurements were performed before and after the CV experiments at the open-circuit potential using a 10 mV amplitude from 100 KHz to 1 Hz. CP was performed for 30 and 50 cycles, with 10 min stripping/deposition intervals, and a current density of 0.1 mA. GITT experiments were done using 15 cycles of CP as done previously, followed by 50 cycles charging at 0.1 mA/cm^2 for 1 min and a 3-min rest period and 50 cycles discharging at –0.1 mA/cm^2 for 1 min and a 3-min rest period.

Material Characterization: SEM images and EDX spectra and maps were recorded taken using a JEOL 7800FLV microscope at 20 kV operating voltage equipped with a field emission electron source and an Oxford XMaxN 80mm² silicon-drift energy-dispersive X-ray spectrometer. EDX data was processed using Oxford Aztec v3.3 software. Raman spectroscopy was performed using a Renishaw inVia Raman microscope, with a 785 nm laser at 50× magnification while flushing with nitrogen, samples were removed from the argon box while in a sealed container and were placed in the Raman microscope as quickly as possible.

XPS was performed on a Kratos Axis Ultra using a monochromatic Al source at an emission of 10 mA and a voltage of 14 KeV with air free sample transfer. Collected spectra were corrected for charging by referencing the C(1s) peak to 284.8 eV. All peaks were fitted in Casa XPS[38] with the Shirley-type background. Powder X-ray diffraction (XRD) data were collected on a Panalytical Empyrean diffractometer at a power of 1.8 kW (45 kV, 40mA) with Cu Ka (l¼1.5418 nm) radiation. The detector was an X'Celerator Scientific, a position sensitive 1D detector equipped with Bragg–Brentano HD X-ray optic delivering only Kα radiation. Patterns were collected with a sampling step of 0.020 and a scan rate of 0.080s while spinning the sample stage at a rate of 0.25 Hz.

ASSOCIATED CONTENT

Supporting Information. XRD data, EDX spectrum, XPS data, tabulated overpotentials for Mg deposition and stripping, Additional CV & CP data, EIS fitting parameters, GITT data, and photograph/description of the electrochemical cells. This material is available free of charge via the Internet at http://pubs.acs.org.

AUTHOR INFORMATION

Corresponding Author

* e-mail: bartmb@umich.edu

Author Contributions

The manuscript was written through contributions of all authors. All authors have given approval to the final version of the manuscript. †These authors contributed equally.

ACKNOWLEDGMENT

This research was supported by a grant from the National Science Foundation, Division of Materials Research, Solid-State Materials Chemistry Program, under Award DMR-1807687. The authors acknowledge the financial support of the University of Michigan College of Engineering and NSF grant #DMR-0420785, and technical support from the Michigan Center for Materials Characterization. Also, the authors would like to acknowledge Jake O'Hara for his artistic work in creating Scheme 1. A special acknowledgement is also made to Dr. Allen Hunter and Dr. Nancy Muyanja for their help with setting up the air-free XPS experiment.

REFERENCES

[1] Trahey, L.; Brushett, F. R.; Balsara, N. P.; Ceder, G.; Cheng, L.; Chiang, Y.; Hahn, N. T.; Ingram, B. J.; Minteer, S. D. ; Moore, J. S. ; Mueller, K. T.; Nazar, L. F.; Persson, K. A.; Siegel, D. J.; Xu, K.; Zavadil, K. R.; Srinivasan, V.; Crabtree, G. W. Energy storage emerging: A perspective from the Joint Center for Energy Storage Research. *Proc. Natl. Acad. Sci. U. S. A.* **2020**, *117*, 12550-1557 DOI: 10.1073/pnas.1821672117.

[2] Huie, D. M. M. ; Bock, C.; Takeuchi, E. S.; Marschilok, A. C.; Takeuchi, K. J. Cathode materials for magnesium and magnesium-ion based batteries. *Coord. Chem. Rev.* **2015**, *287*, 15-27. DOI: 10.1016/j.ccr.2014.11.005.

[3] Yoo, H. D.; Shterenberg, I.; Gofer, Y.; Gershinsky, Pour, N.; Aurbach, D. Mg rechargeable batteries: an on-going challenge. *Energy Environ. Sci.* **2013**, *6*, 2265-2269. DOI: 10.1039/C3EE40871J

[4] Fichtner, M. Magnesium Batteries Research and Applications. The Royal Society of Chemistry, **2019**, pp 1-16.

[5] Biemolt, J.; Jungbacker, P.; Teijlingen, T. V.; Yan, N.; Rothenberg, G. Beyond Lithium-Based Batteries. *Materials* **2020**, *13*, 425. DOI: 10.3390/ma13020425

[6] Mohtadi, R.; Mizuno, F.; Magnesium batteries: Current state of the art, issues and future perspectives. *Beilstein J. Nanotechnol.* **2014**, *5*, 1291-1311. DOI: 10.3762/bjnano.5.143

[7] Zhao-Karger, Z.; Fichtner, M. Beyond Intercalation Chemistry for Rechargeable Mg Batteries: A Short Review and Perspective. *Front. Chem.* **2019**, *6*, 656. DOI 10.3389/fchem.2018.00656.

[8] Deivanayagam, R.; Ingram, B. J.; Shahbazian-Yassar, R. Progress in development of electrolytes for magnesium batteries. *Energy Stor. Mater.* **2019**, *21*, 136-153.DOI: 10.1016/j.ensm.2019.05.028.

[9] Muldoon, J.; Bucur, C. B.; Oliver, A. G.; Sugimoto, T.; Matsui, M.; Kim, H. S.; Allred, G. D.; Zajicek, J.; Kotani, Y. Electrolyte roadblocks to a magnesium rechargeable battery. *Energy Environ. Sci.* **2012**, *5*, 5941-5950. DOI: 10.1039/C2EE03029B.

[10] Attias, R.; Salama, M.; Hirsch, B.; Goffer, Y.; Aurbach, D.; Attias, R.; Salama, M.; Hirsch, B.; Goffer, Y.; Aurbach, D. *Joule.* **2019**, *3*, 27-52. DOI: 10.1016/j.joule.2018.10.028.

[11] Aurbach, D.; Lu, Z.; Schechter, A.; Gofer, Y.; Gizbar, H.; Turgeman, R.; Cohen, Y.; Moshkovich, M.; Levi, E. Prototype systems for rechargeable magnesium batteries. *Nature* **2000**, *407*, 724-727. DOI: 10.1038/35037553.

[12] Mizrahi, O.; Amir, N.; Pollak, E.; Chusid, O.; Marks, V.; Gottlieb, H.; Larush, L.; Zinigrad, E.; Aurbach, D. Electrolyte Solutions with a Wide Electrochemical Window for Rechargeable Magnesium Batteries. *J. Electrochem. Soc.* **2008**, *155*, A103. DOI 10.1149/1.2806175.

[13] Nist-Lund, C. A.; Herb, J. T.; Arnold, C. B. Improving halide-containing magnesium-ion electrolyte performance via sterically hindered alkoxide ligands. *J. Power Sources* **2017**, *362*, 308-314. DOI: 10.1016/j.jpowsour.2017.07.045

[14] Guo, Y.; Zhang, F.; Yang, J.; Wang, F.; Nuli, Y.; Hirano, S. Boron-based electrolyte solutions with wide electrochemical windows for rechargeable magnesium batteries. *Energy Environ. Sci.* **2012**, *5*, 9100-9106. DOI: 10.1039/C2EE22509C

[15] Crowe, A. J.; Stringham, K. K.; Bartlett, B. M.; Fluorinated Alkoxide-Based Magnesium-Ion Battery Electrolytes that Demonstrate Li-Ion-Battery-Like High Anodic Stability and Solution Conductivity. *ACS Appl. Mater. Interfaces* **2016**, *8*, 23060-23065. DOI: 10.1021/acsami.6b07262

[16] Muldoon, J.; Bucur, C. B.; Oliver, A. G.; Zajicek, J.; Allred, G. D.; Boggess, W. C. Corrosion of magnesium electrolytes: chlorides –

the culprit. *Energy Environ. Sci.* **2013**, *6*, 482487. DOI: 10.1039/C2EE23686A

[17] Crowe, A. J. Stringham, K. K.; Dimeglio, J. L.; Bartlett, B. M. Adsorption of Aromatic Decomposition Products from Phenyl-Containing Magnesium-Ion Battery Electrolyte Solutions. *J. Phys. Chem. C* **2017**, *121*, 7711-7717. DOI: 10.1021/acs.jpcc.7b00813

[18] Sato, K.; Mori, G.; Kiyosu, T.; Yaji, T.; Nakanishi, K.; Ohta, T.; Okamoto, K.; Orikasa, Y. Improved Non-Grignard Electrolyte Based on Magnesium Borate Trichloride for Rechargeable Magnesium Batteries. *Sci. Rep.* **2020**, *10*, 7262- DOI 10.1038/s41598-020-64085-2.

[19] Barile, C. J.; Barile, E. C.; Zavadil, K. E.; Nuzzo, R. G.; Gewirth, A. A. Electrolytic Conditioning of a Magnesium Aluminum Chloride Complex for Reversible Magnesium Deposition. *J. Phys. Chem. C* **2014**, *118*, 27623-27630. DOI: 10.1021/jp506951b.

[20] Wang, P.; Buchmeiser, M. R. Rechargeable Magnesium–Sulfur Battery Technology: State of the Art and Key Challenges. *Adv. Funct. Mater*. **2019**, *29*, 1905248. DOI: 10.1002/adfm.201905248.

[21] Jay, R.; Tomich, A. W.; Zhang, J.; Zhao,Y.; Gorostiza, A. D.; Lavallo, V.; Guo, J.; Comparative Study of $Mg(CB_{11}H_{12})_2$ and $Mg(TFSI)_2$ at the Magnesium/Electrolyte Interface. *ACS Appl. Mater. Interfaces* **2019**, *11*, 11414-114120. DOI: 10.1021/acsami.9b00037

[22] Lu, Z. Schechter, A.; Moshkovich, M.; Aurbach, D.; On the electrochemical behavior of magnesium electrodes in polar aprotic electrolyte solutions. *J. Electroanal. Chem.* **1999**, *466*, 203-217. DOI: 10.1016/S0022-0728(99)00146-1.

[23] Yoo, H. D.; Han, S.; Bolotin, I. L.; Nolis, G. M.; Bayliss, R. D.; Burrell, A. K.; Vaughey, J. T.; Cabana. J. Degradation Mechanisms of Magnesium Metal Anodes in Electrolytes Based on $(CF_3SO_2)_2N^-$ at High Current Densities *Langmuir* **2017** *33*, 37, 9398-9406. DOI : 10.1021/acs.langmuir.7b01051.

[24] Tang, K. ; Du, A.; Dong, S. ; Cui, Z. ; Liu, X. ; Lu, C. ; Zhao, J. ; Zhou, X. ; Cui, G. A Stable Solid Electrolyte Interphase for Magnesium Metal Anode Evolved from a Bulky Anion Lithium Salt. *Adv. Mater.* **2020**, 32, 1904987. DOI: 10.1002/adma.201904987.

[25] Son, S.; Gao, T.; Harvey, S. P.; Steirer, K. X.; Stokes, A.; Norman, A.; Wang, C.; Cresce, A.; Xu, C.; Ban, C. An artificial interphase enables reversible magnesium chemistry in carbonate electrolytes. Nat. Chem**. 2018**, *10*, 532-539. DOI: 10.1038/s41557-018-0019-6.

[26] Li, B.; Masse, R.; Liu, C.; Hu, Y.; Li, W.; Zhang, G.; Cao, G. Kinetic surface control for improved magnesium-electrolyte interfaces for magnesium ion batteries. *Energy Stor. Mater.* **2019**, *22*, 96-104. DOI: 10.1016/j.ensm.2019.06.035.

[27] Li, X.; Gao, T.; Han, F.; Ma, Z.; Fan, X.; Hou, S.; Eidson, N.; Li, W.; Wang, C. Reducing Mg Anode Overpotential via Ion Conductive Surface Layer Formation by Iodine Additive. *Adv. Energy Mater*. **2018**, *8*, 1701728. DOI: 10.1002/aenm.201701728.

[28] Parambath, V. B.; Zhao-Karger, Z.; Diemant, T.; Jäckle, M.; Li, Z.; Scherer, T.; Gross, A.; Behm, R. J.; Fichtner, M. Investigation on the formation of Mg metal anode/electrolyte interfaces in Mg/S batteries with electrolyte additives. *J. Mater. Chem. A* **2020**, *8*, 22998-23010. DOI: 10.1039/D0TA05762B

[29] Ahsan, M. S.; Kochetov, V.; Hein, D.; Bokarev, S. I.; Wiklinson, I. Probing the molecular structure of aqueous triiodide via X-ray photoelectron spectroscopy and correlated electron phenomena. *Phys. Chem. Chem. Phys.*, **2022**, 24, 15540-15555. DOI: 10.1039/D1CP05840A.

[30] Momma, K.; Izumi, F. VESTA 3 for three-dimensional visualization of crystal, volumetric and morphology data. *J. Appl. Crystallogr.* **2011,** *44*, 1272-1276. DOI: 10.1107/S0021889811038970

[31] Hanwell, M. D.; Curtis, D. E.; Lonie, D. C.; Vandermeersch, T.; Zurek R. Hutchison, G. R. Avogadro: An advanced semantic chemical editor, visualization, and analysis platform. *J. Cheminf.* **2012**, *4,* 17. 1-17. DOI: 10.1186/1758-2946-4-17.

[32] Tian, H.; Gao, T.; Li, X.; Wang, X.; Luo, C.; Fan, X.; Yang, C.; Suo, L.; Ma, Z.; Han, W.; Wang, C. High power rechargeable magnesium-iodine battery chemistry. *Nature Commun.* **2017**, *8*, 14083. DOI: ncomms14083.

[33] Prabhakaran, V.; Agarwal, G.; Howard, J. D.; Wi, S.; Shutthanandan, V.;Nguyen, D.; Soule, L.; Johnson, G. E.; Liu, Y.; Yang, F.; Feng, X.; Guo, J.; Hankins, K.; Curtiss, L. A.; Mueller, K. T.; Assary, R. S.; Murugesan, V. Coordination-Dependent Chemical Reactivity of TFSI Anions at a Mg Metal Interface. *ACS Appl. Mater. Interfaces* **2023**, 15, 5, 7518-7528. DOI: 10.1021/acsami.2c18477

[34] Nakabayshi, Y.; Saito, M.; Kanamura, K. Effect of EtOMgCl Salt to Suppress Reductive Decomposition of TFSI− Anion in Electrolyte for Magnesium Rechargeable Battery. *J. Electrochem. Soc. Jpn.* **2022**, 30, 037010. DOI: 10.5796/electrochemistry.21-00124.

[35] Bard, A. J.; Faulkner, L. R. Double-Layer Structure and Absorption. In Electrochemical Methods: Fundamentals and Applications, 2nd ed.; John Wiley & Sons, 2001; pp 471-528.

[36] *Scribner Associates Release 2019-2: ZView;* Scribner Associates, Inc: North Carolina, 2019. https://www.scribner.com/software/68-general-electrochemistr376-zview-for-windows/

[37] Crowe, A. J.; Dimeglio, J. L.; Stringham, K. K.; Bartlett, B. M. Kinetics of Magnesium Deposition and Stripping from Non-Aqueous Electrolytes. *J. Phys. Chem. C* **2017**, *121*, 20613-20620. DOI: 10.1021/acs.jpcc.7b06068

[38] Fairley, N.; Fernandez, V.; Richard-Plouet, M.; Guillot-Deudon, C.; Walton, J.; Smith, E.; Flahaut, D.; Greiner, M.; Biesinger, M.; Tougaard, S.; Morgan, D.; Baltrusaitis, J. Systematic and collaborative approach to problem solving using X-ray photoelectron spectroscopy. *Applied Surface Science Advances.* **2021,** *5*, 100112. DOI: 10.1016/j.apsadv.2021.100112.

Insert Table of Contents artwork here